# Infrared heating modeling of recycled PET preforms in injection stretch blow molding process

Anh-Duc Le, Rémi Gilblas, Vincent Lucin, Yannick Le Maoult, Fabrice Schmidt

# Infrared heating modeling of recycled PET preforms in injection stretch blow molding process

Anh-Duc Le, Rémi Gilblas *, Vincent Lucin, Yannick Le Maoult, Fabrice Schmidt

*Université de Toulouse, IMT Mines Albi, ICA (Institut Clément Ader), Campus Jarlard, Albi cedex 09, F-81013, France*

A B S T R A C T

Relatively recent citizen's consciousness about plastic pollution forces industrial actors of packaging to re-invent their shaping processes and materials. Specifically, for plastic bottle industry shaping, classical Polyethylene Terephthalate (PET) material is little by little replaced by recycled PET (rPET). The change in material composition due to recycling loops leads to an inevitable adaptation of the Injection Stretch Blow Molding (ISBM) process used to shape bottles at a satisfactory production rate. Indeed, rPET contains contaminants which modify its optical properties, so the heating stage becomes material-dependent and unstable regarding the polymer supplier. The approach adopted in this article is to build a numerical model able to simulate the infrared heating of rPET preforms, sensitive enough to predict changes in temperature due to the recycling rate. To do so, the optical properties of 50% and 100% rPET are measured by spectrometry and implemented in the simulation. Thermal radiative heat transfer between infrared lamps and rPET preforms is simulated by ray tracing method using an in-house software so-called RAYHEAT. Then, the result of the infrared ray tracing computation is used as the input heat source for thermal simulation by commercial software COMSOL Multiphysic® in order to simulate the temperature distribution of the preform. The numerical results are then confronted to experimental ones obtained on a research Stretch Blow Molding pilot, instrumented with thermography. The results show that the temperature obtained at the end of a classical heating cycle of the 100% recycled grade is 8 °C higher than the virgin one. Also, simulations confirm that this difference is attributed to changes in optical properties. Finally, heating 100% rPET at a sufficient forming temperature is about 8% less energy consuming than for virgin PET.

## 1. Introduction

Nowadays, the most employed technology to produce plastic bottles is based on two-stages ISBM process. In the first stage, the process starts with a classical injection molding to produce a tube-like preform. In the second stage, so-called Stretch Blow Molding (SBM), the preforms are transferred into an infrared (IR) oven where they are heated above the glass transition temperature but just under the crystallization temperature of the resin to avoid making the transparent amorphous preform completely opaque and more fragile. Then, the heated preforms are transferred into a mold, where they are stretched axially by a rod and radially by compressed air until it takes up the shape of the bottle mold.

The ISBM process is now well mastered, but its performances are subjected to the homogeneity of the properties of the polymer resin introduced at the beginning of the production chain. PET has been pointed out as one of the most widely used plastic in the packaging industry because of its chemical, physical and mechanical properties and its negligible permeability to $CO_2$ [1], which are very relevant for packaging applications.

Virgin PET has been adapted for usage in ISBM process since the 1980s. Recently, the use of rPET in bottles has increased largely since the emergence of a citizen's conscience on plastic pollution [2]. Furthermore, the use of rPET as an alternative to virgin PET or glass-made bottles significantly rose up in the last decades due to its considerably recyclability [3]. However, the introduction of recycled content induces important variability in the composition of the input resin, which are *a priori* uncontrollable when subjected to the diversity of collection sources, as well as to multiple recycling loops. In order to achieve a higher content of rPET used in bottles, it is essential to make the ISBM process more robust with respect to the composition of the input resins.

This study is focused on the simulation of IR heating of rPET preforms in ISBM process. Actually, IR heating process is determined by controlling the geometrical and spectral interactions between IR lamps and reflectors constituting the oven and irradiated plastic materials. Many works in literature highlighted that the temperature distribution inside the preform prior to forming is of prime importance to improve

* Corresponding author.
*E-mail address:* remi.gilblas@mines-albi.fr (R. Gilblas).

the production quality of PET bottles [4–8]. This is explained by the fact that this temperature distribution has a significant impact on the visco-plastic properties of PET during forming and, thus on the dynamics of the SBM phase, which determine the final thickness distribution of the bottle. Previous works showed that the optimal temperature distribution is hard to obtain experimentally [9,10]. Additionally, rPET represents variability of optical properties due to contaminants and recycling process. The efficiency of IR heating of rPET preforms thereby becomes material-dependent regarding recycling rate. From an industrial point of view, it is extremely important to figure out the energy cost of ISBM machines with respect to the input resins.

To face these issues, a numerical approach is introduced by using a ray tracing method, aiming at studying the effects of recycled content in the input resins on the temperature distribution of rPET preforms. The chosen method allows modeling of radiative energy absorption inside the semi-transparent materials, and more especially, is sensitive enough to predict changes in temperature due to the recycling rate.

The methodology used in this study is well established in the literature [7,11,12]. However, the novelty of this work is the further improvements of the IR heating model and its application to the recycled PET preforms. This improvement is carried out following three aspects: Firstly, the characterization of the optical properties depending on the impact of the recycling rate is conducted. The second step is an improvement of the natural convective model, which is taken into account using two different approaches: the first one uses a correlated heat transfer coefficient, $h$, for a vertical thin cylinder in a laminar flow regime, and the second one uses a multiphysics approach by coupling computational fluid dynamics (CFD) and heat transfer. Finally, the influence of the differences in optical properties on the resultant temperature field is evaluated through a numerical/experimental confrontation. It is the basis of an advanced energy balance study at the level of an industrial machine, which is little by little impacted by the recycling issues.

As a first step, the optical properties of the materials are measured using spectrometry. Also, the IR heaters are characterized in order to find out the associated emitted power and wavelength range. Then, simulations composed of ray tracing method are performed in order to calculate the volumetric heat sources absorbed inside the preforms due to IR heating, and loaded as boundary conditions for thermal simulations in the commercial software COMSOL Multiphysic®. With the aim of a more accurate thermal analysis, the model also takes into account the heat exchange with the support which is often lacking from the recent works [7,11]. The numerical model successfully predicts the differences in the temperature distribution through rPET preforms of different recycled grades, which is attributed to changes in the optical properties. Finally, simulated results provide necessary elements to estimate the energy cost for the industrial ISBM machines with respect to the recycling rate of the input rPET.

## 2. Material properties and optical characterization

### 2.1. Material description

Preforms used in this study are made from two grades of rPET with recycled contents of 50% and 100%, and virgin PET resin materials. The rPET materials were collected from Europe. Virgin PET RAMAPET $N180$ was supplied by Indorama Ventures Europe. The rPET was mixed with virgin PET in weight ratios of 50:50% to produce the recycled grade 50% rPET. All preforms were produced by injection molding under identical conditions. The preforms used are 18.5 g weight, and 2.55 mm thickness, provided by the SIDEL company, partner in the CARNOT 2020 AAP 2 BOUTEILLE project.

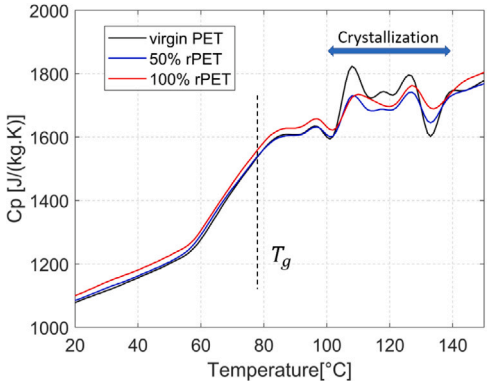


**Fig. 1.** Specific heat capacity vs. temperature.

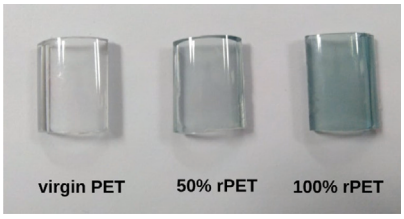


**Fig. 2.** Samples for spectrometry.

### 2.2. Thermal properties

The density of polymer is measured by use of a double balance, which showed a very small dispersion between virgin and recycled grades. For this reason, an average value is taken for all types: $\overline{\rho} = 1.335 \pm 1e^{-3}$ kg m$^{-3}$. Also, the thermal conductivity of polymer is assumed to be constant for both virgin and recycled grades: $\overline{k} = 0.25$ W m$^{-1}$ K$^{-1}$ [13]. Measurements of the specific heat capacity of the materials are carried out by Differential Scanning Calorimetry using a Perkin Elmer calorimeter. Measurements are performed under an inert nitrogen atmosphere between 20 °C and 150 °C, heating rate is set at 5 °C per minute. Fig. 1 reveals a small dispersion between virgin and recycled grades (i.e. less than 1.2% for the 50% rPET and less than 2.5% for the 100% rPET in comparison with the virgin one). Under heating conditions, $C_p$ is not strictly monotonic but exhibits a phase transition related to the crystallization kinetic of the polymers between 100 °C and 140 °C. In this application for the ISBM process, the heating stage is performed until the preforms get a sufficient temperature just under the crystallization temperature to avoid making the transparent amorphous preform completely opaque and more fragile. For this reason, the crystallization kinetic is not modeled and $C_p(T)$ is directly used as an input in the numerical model.

### 2.3. Optical properties characterization

The optical properties have a direct influence on the radiative absorption and emission phenomena of PET, and thus on the efficiency of the IR heating process. The introduction of recycled content results in a variability in the composition of the input resin. Accordingly, it is highly probable that the optical properties of the polymer will be impacted. The intrinsic transmissivity ($\tau_\lambda$), and reflectivity ($\rho_\lambda$) coefficients of semi-transparent polymers are determined from measurements of the transmission factor ($T_\lambda$) and the reflection factor ($R_\lambda$). These measurements have been done using a Fourier Transform Infrared spectrometer (FT-IR Bruker Vertex 70) over the spectral range [0.4 – 25] μm. Considering that the reflection of light on the surface of the polymer is specular, and that the optical scattering transport inside

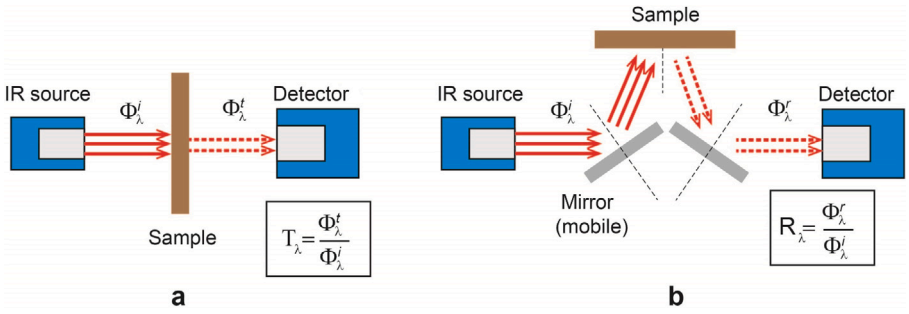


**Fig. 3.** Schematic representations of the experimental measurement setups of FT-IR spectrometer.(a) Transmission measurement; (b) Reflection measurement..

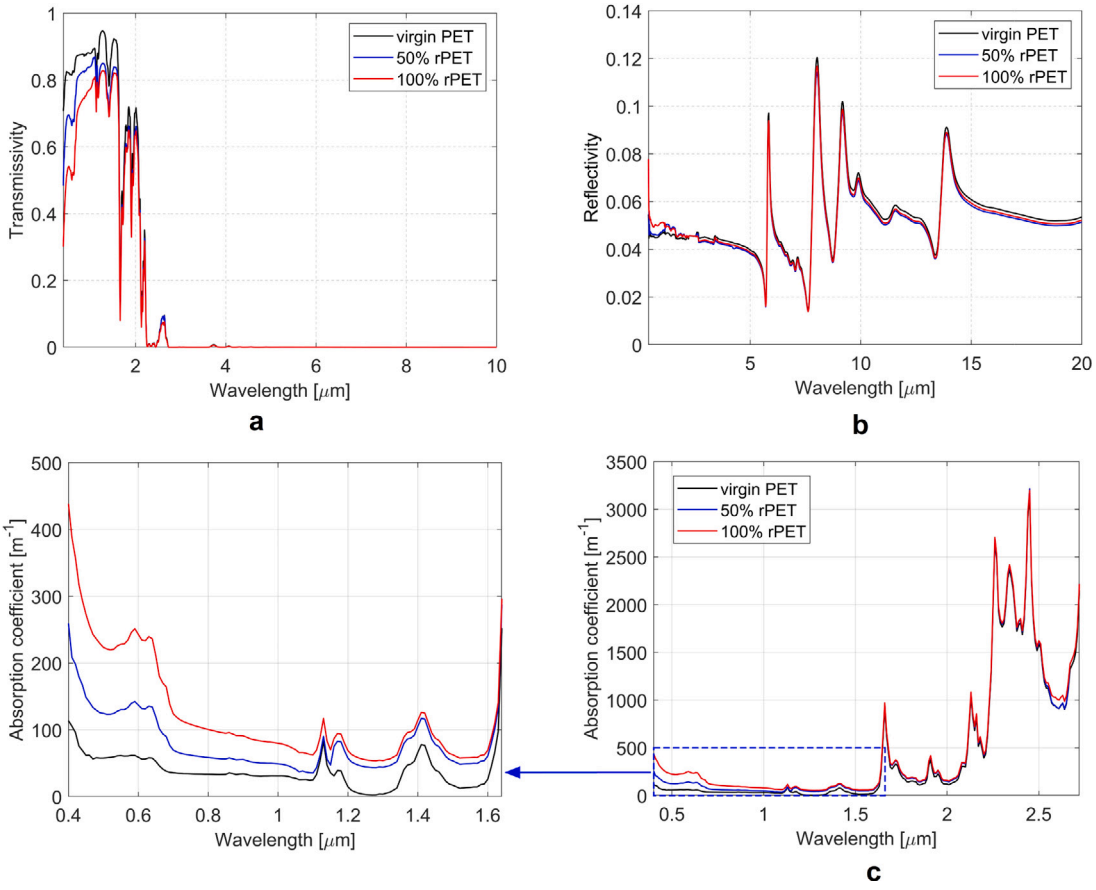


**Fig. 4.** (a) Transmissivity vs. wavelength; (b) Reflectivity vs. wavelength; (c) Absorption coefficient vs. wavelength.

of polymer medium is neglected. The fundamentals of the experimental measurement setups are sketched in Fig. 3. The samples, 2.55 mm thick rectangular sheets, are obtained by cutting directly from the tubular preforms, at the flattest possible position as can be seen in Fig. 2.

The semi-transparency nature of rPET, especially in the visible and near-infrared range, leads to the thickness-dependent measurement of radiative properties. The preforms can be modeled as two diopters medium, where the apparent reflection (and transmission) is a combination of the reflection (and transmission) at the first interface and at the second interface, after attenuation in the volume. Thus, the measured data of transmission ($T_\lambda$) and reflection factors ($R_\lambda$) are functions of the intrinsic coefficients ($\tau_\lambda$) and ($\rho_\lambda$). The expressions of these quantities can be found in the literature [14], whose approach is based on the conservation of radiative energy (Eqs. (1) and (2)):

$$T_\lambda = \frac{\left(1-\rho_\lambda\right)^2 \tau_\lambda}{1-\left(\rho_\lambda \tau_\lambda\right)^2} \tag{1}$$

$$R_\lambda = \rho_\lambda + \frac{\left(1-\rho_\lambda\right)^2 \rho_\lambda \tau_\lambda^2}{1-\left(\rho_\lambda \tau_\lambda\right)^2} \tag{2}$$

A numerical approach is then used to identify the material intrinsic coefficients ($\tau_\lambda$) and ($\rho_\lambda$) from the apparent coefficients ($T_\lambda$) and ($R_\lambda$), which is based on an inverse method for nonlinear optimization [15]. In this method, the values of these material intrinsic coefficients are identified by using a SQP (Sequential Quadratic Programming) estimation algorithm such with the minimization of the objective function $f\left(\tau_\lambda, \rho_\lambda\right)$:

$$\min_X f(X) = \left| \frac{T_\lambda^{\text{experimental}} - T_\lambda^{\text{numerical}}(X)}{T_\lambda^{\text{experimental}}} \right| + \left| \frac{R_\lambda^{\text{experimental}} - R_\lambda^{\text{numerical}}(X)}{R_\lambda^{\text{experimental}}} \right| \tag{3}$$

Where $X = [\tau_\lambda, \rho_\lambda]$, $T_\lambda^{\text{experimental}}$ and $R_\lambda^{\text{experimental}}$ are the measured data of transmission and reflection factors.

$T_\lambda^{\text{numerical}}(X)$ and $R_\lambda^{\text{numerical}}(X)$ are the numerical values computed according to Eqs. (1) and (2) at each iteration. The solutions are reached when the solver error condition is satisfied at which the value of $f(X)$ is smaller than a predefined tolerance (i.e. $1e-6$). Under the assumption that PET is a non-scattering and cold medium [16], the transmissivity coefficient ($\tau_\lambda$) is given according to the Beer–Lambert law (Eq. (4)):

$$\tau_\lambda = \left(1 - \rho_\lambda\right) e^{-\kappa_\lambda d} \tag{4}$$

where $\kappa_\lambda$ stands for the absorption coefficient, and $d$ is the sample thickness. The determination of $\kappa_\lambda$, which is independent of $d$, requires at least three samples of different thicknesses. The further details related to this protocol can be found in Ref. [17]. However, in this work only one type of preform was used, whose thickness is almost uniform $d = 2.55$ mm, the absorption coefficient ($\kappa_\lambda$) can be calculated directly from the computation result of the transmissivity coefficient ($\tau_\lambda$) according to Eq. (4). In Fig. 4, the transmissivity ($\tau_\lambda$), the reflectivity ($\rho_\lambda$) and the absorption coefficient ($\kappa_\lambda$) are plotted versus wavelength for the three PET grades. It is important to note that, for all grades, the transmission is low in the spectral range $[2.72 - 25]$ μm. This means that all the radiative energy emitted in this specific wavelength range is completely absorbed by the preforms used in this study. For this reason, the computation of the absorption coefficient is not available in this spectral range, and thus is not plotted in Fig. 4c. Furthermore, it is clearly seen that the differences in optical properties of the resins due to effects of recycled content are mostly found in the visible and near-infrared (NIR) spectra, including the spectrum between 0.4 and 1.65 μm. Considering a quartz tungsten halogen lamp used for injection stretch blow molding (ISBM) processes, the primary source, tungsten filament, has a temperature around 1800–2600 K, the maximum emission wavelength ($\lambda_{max}$) of the filament can be theoretically found around $[1.1 - 1.6]$ μm, regarding to Wien's displacement law [14]. Then the percentage of radiative energy emitted up to 1.65 μm can be theoretically found between 26%(1800 K) and 52% (2600 K) according to Planck's law [14]. Therefore, it is straightforward to show that the variation in absorption characteristics in the spectral range $[0.4 - 1.65]$ μm may have a significant effect on the amount of absorbed energy and, consequently, on the efficiency of the IR heating stage.

The origin of the above-mentioned variabilities in material properties of rPET remains uncertain, which can be caused by the presence of contaminants combined with the changes in the microstructure of rPET during the recycling process. Further tests were carried out within the framework of the project CARNOT 2020 AAP 2 BOUTEILLE, using conventional analysis methods (i.e. X-ray Photoelectron Spectroscopy (XPS), Energy Dispersive Spectroscopy (EDS), IR spectroscopy, or DSC). In conclusion, contaminants content is very low and always under the detection thresholds of the equipment. However, the presence of shorter chains in rPET due to the scission of molecular chains during the recycling process may be the main cause of variability.

## 3. Experimental set-up

### 3.1. Presentation of the blow molding set-up

The experimental set-up on the SBM prototype which has been developed in ICA laboratory is shown in Fig. 5. For this application, the oven is constituted of six quartz tungsten halogen lamps (Toshiba lighting 1000 W-235 V) and a flat white ceramic reflector located behind the lamps. Nominal percentage powers of each lamp are reported in Table 1. The preform is heated during 50 s and then cooled down by natural convection during 10 s. During the heating stage, the preform can rotate axially in the middle of the oven. This is of critical importance to ensure a uniform heating through the preform circumference. The rotational speed is $\omega = 1.15$ rotation per second. The oven is open throughout the experiments, where the air can circulate freely. Thus, the heating of the air by convection and radiation is considered to be negligible.

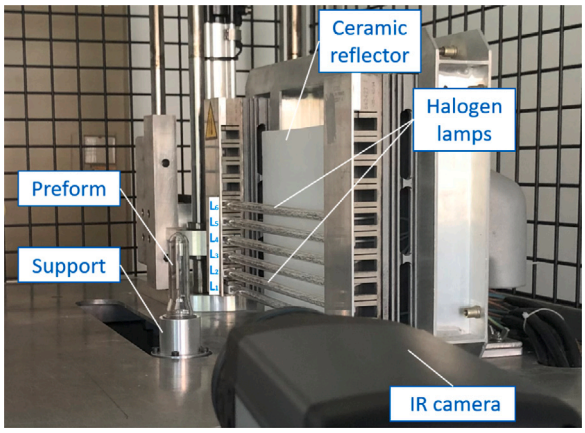


**Fig. 5.** In-lab IR oven.

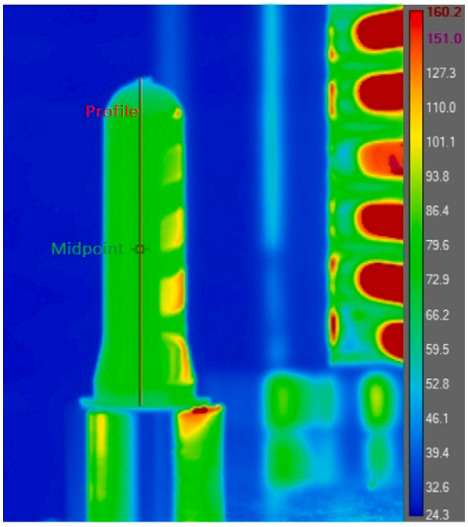


**Fig. 6.** Experimental thermography image.

**Table 1**
Nominal electrical powers of lamps setting for experimental set-up.

| Lamp | $L_1$ | $L_2$ | $L_3$ | $L_4$ | $L_5$ | $L_6$ |
|---|---|---|---|---|---|---|
| Nominal power | 100% | 100% | 45% | 30% | 75% | 90% |

### 3.2. Thermography temperature measurement

A FLIR A655sc IR camera, operating in the spectral range $[7.5 - 14]$ μm have been chosen for measuring the surface temperature of the preform. Thermographic images were recorded at 2 frames/s. Fig. 6 shows a typical image of thermography measurement. The reflection of the lamps is visible on the right side of the preform. Therefore, measurements were performed slightly aside to the left side to avoid this effect. For each material grades, repeated measurements were conducted 5 times.

As it can be seen in Fig. 4 above, over the spectral range $[7.5 - 14]$ μm, transmissions are low for all PET grades. This means that preforms can be *a priori* considered as opaque in this specific spectral range, so that surface temperature measurement can be performed [18]. Furthermore, reflectivity measurements showed a very small dispersion between virgin and recycled grades (i.e. less than 0.2% over the spectral range $[7.5 - 14]$ μm), with low integrated values (i.e. approximately 6% for all grades). For this reason, an average emissivity of 0.94 is taken for all measurements. This value corresponds to

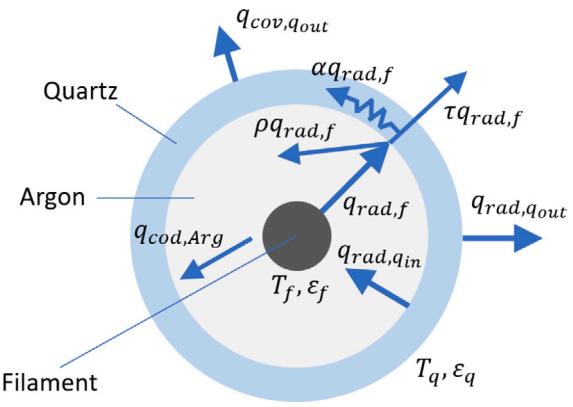


**Fig. 7.** Diagram of quartz tungsten halogen lamp and heat transfer mechanisms.

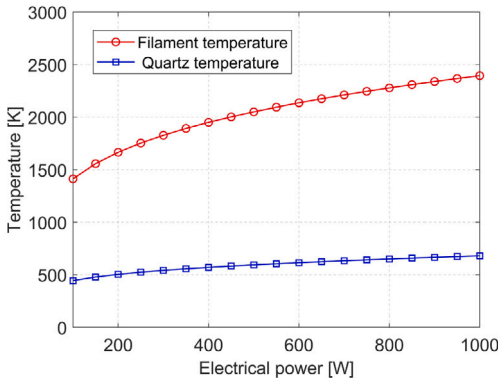


**Fig. 8.** Filament and quartz tube temperatures vs. electrical power computed.

the integration of the spectral emissivity of the resins over the operating spectral range of the IR camera. To sum up, even though recycling rate has a strong influence on the visible optical properties, it has no influence in the infrared, so on the thermography measurement setting (i.e. infrared emissivity). The measurement uncertainty is provided by the IR camera supplier (FLIR®) and is equal to maximum ±2 °C in the thermal range [20 – 120] °C. This value is then used in the experimental section part to build error bars.

### 3.3. Heat source characterization

Accurate modeling of radiative heat transfer emitted from the lamps requires knowledge about the operating temperatures of each element (i.e. tungsten filament and quartz tube), which depend proportionally on the electrical power input to the lamps. This is because they affect the maximum power and wavelength range associated with the elements [16]. These operating temperatures can be obtained either by experimental measurements [19,20], or by numerical calculations [21–23]. Considering that the temperature of the tungsten filament is very high in comparison to the temperature of the quartz tube, several previous studies made the assumption that the tungsten filament is the sole radiation source, the radiation emitted from the quartz tube is neglected [11,22,24]. Moreover, the authors assumed that losses due to convection and conduction within the lamps are negligible, thus the lamps converted 100% of the electrical power input to radiation [11, 22]. Conversely, several works showed a significant contribution of the quartz tube to the sum of the radiative transfers, which was taken into account as an additional source of radiation [12,17,25]. The research of Monteix et al. [17] concluded that the participation of quartz tube amounts to 9% of the total radiative energy emitted from the tungsten filament.

Based on the literature discussed, in this work, each lamp is considered to be composed of two sources, the filament and the quartz tube. The filament is the primary source, while the quartz tube is the secondary source, acquiring its energy via the combined effects of conduction and absorption of energy radiated from the filament. The determination of the tungsten filament and quartz tube temperatures according to the supplied electrical power is performed using an easy and quick net radiation method [12]. The quartz tube is treated as a partially reflecting, transmitting, and absorbing medium. It is also assumed a uniform temperature throughout its thickness. A cross section of the lamp geometry with heat transfer mechanisms is illustrated in Fig. 7. Thank to the symmetry of the lamp geometry in the length direction, the analysis is simplified to be essentially two dimensional. An energy balance at steady state is established for heat transfer for all components of the lamps (Eq. (5)). The further details related to the development of the energy balance can be found in Refs. [12,17].

$$\begin{cases} P - q_{rad,f} + \varepsilon_f\left(T_q\right) F_{q-f} q_{rad,q_{in}} \\ +F_{q-f}\rho_q\left(T_f\right) F_{f-q} q_{rad,f} - q_{cod,Arg} = 0, \\ \alpha_q\left(T_f\right) F_{f-q} q_{rad,f} + q_{cod,Arg} - q_{rad,q_{out}} \\ -q_{rad,q_{in}} + q_{\mathrm{cov},q_{out}} = 0 \end{cases} \tag{5}$$

where P is the input electrical power supplied to the lamp, $q_{rad,f}$ stands for the total radiative heat flux emitted from the tungsten filament surface, $q_{rad,q_{in}}$ and $q_{rad,q_{out}}$ are the total radiative heat flux emitted from the inner and outer surfaces of the quartz tube respectively. $q_{cod,Arg}$ represents the total conductive heat flux from the filament to the quartz tube through the gas Argon, and $q_{\mathrm{cov},q_{out}}$ is the total convective heat flux at the outer surface of the quartz tube. $F_{f-q}$ and $F_{f-q}$ stand for the view factors between the filament surface and the inner surface of the quartz tube, and vice versa. $\varepsilon$, $\rho$, and $\alpha$ represent the integrated radiative parameters: emissivity, reflectivity and absorptivity of the materials respectively. The subscripts $f$ and $q$ are used to refer the optical properties of tungsten filament and quartz tube respectively. These optical properties as polynomial functions depending on the temperatures have already been characterized in previous works [5,17].

As the lamp filament consists of a large number of components which are very close one to the other, its representation in three dimensions has been approximated by a smooth cylinder. However, due to its spiral shape, the filament has a larger total effective emission area than a smooth cylinder. Therefore, the diameter $d_c$ is increased with a factor of $\frac{\pi}{2}$ to reproduce an effective cylinder diameter $d_f = d_c.\frac{\pi}{2}$ as in Ref. [12]. The dimensions of quartz tungsten halogen lamp are listed in Table 2.

**Table 2**
Dimensions of quartz tungsten halogen lamp.

| Parameter | Symbol | Value | Unit |
|---|---|---|---|
| Diameter of tungsten filament | $d_f$ | $1.97 \times 10^{-3}$ | m |
| Diameter of quartz tube | $d_q$ | $10.40 \times 10^{-3}$ | m |
| Thickness of quartz tube | $e_q$ | $1.25 \times 10^{-3}$ | m |
| Length of lamps | $L$ | $272 \times 10^{-3}$ | m |

Finally, the non-linear system Eq. (5) is solved iteratively at steady state using a Newton–Raphson method. The material property data used in this computation can be found in Table 3. The results of the computation are shown in Fig. 8. These results confirm that the temperature of the tungsten filament is very high in comparison to the one of the quartz tube. However, taking into account the fact that the emission surface of the quartz tube is much larger than that of the tungsten filament, the participation in heating of the quartz tube should not be neglected.

**Table 3**
Material properties used in the calculation of $T_f$ and $T_q$ [5,17].

| Property | Symbol | Value | Range |
|---|---|---|---|
| Emissivity of tungsten filament | $\varepsilon_f$ | $-2.8500\times10^{-8}T^2+2.2143\times10^{-4}T-9.2555\times10^{-2}$ | $1500<T<3000$ K |
| Emissivity of quartz | $\varepsilon_q$ | $-7.1336\times10^{-11}T^3+5.3492\times10^{-7}T^2-1.3785\times10^{-3}T+1.2781$ | $400<T<3000$ K |
| Reflectivity of quartz | $\rho_q$ | $5.2869\times10^{-6}T+6.3138\times10^{-2}$ | $400<T<3000$ K |
| Thermal conductivity of Argon | $k_{Argon}$ | $3.61\times10^{-5}T+7.34\times10^{-3}$ W m$^{-1}$ K$^{-1}$ | $300<T<1100$ K |
| Convection coefficient | $h$ | 14 W m$^{-2}$ K$^{-1}$ | – |

## 4. Numerical modeling

### 4.1. Simulation approach

In the present work, a two-stage analysis approach is developed to evaluate the thermal condition of the recycled PET preforms in the IR heating step of the ISBM process. For the first stage of analysis, an in-house developed radiative heat transfer software, so-called RAYHEAT, is used to simulate the IR absorption inside the preform as a source term. Then, this source term induced by infrared radiation inside the preform is loaded as an input for the thermal analysis. The temperature distribution of the preform is evaluated by transient thermal analysis with a finite element commercial software, COMSOL Multiphysic®.

### 4.2. Infrared ray tracing analysis

Thermal radiation computations are performed using the in-house software RAYHEAT. The algorithm is based on ray tracing method where the radiative heat flux from an IR emitter is discretized into a set of rays, then the path of each ray is followed in the model geometry. This method is very close to the physics of light propagation, since a ray can represent the path of a photon. RAYHEAT accounts for a wide variety of optical effects, such as absorption, specular or diffuse reflections and refractions of light. In addition, RAYHEAT enables us to take into account most of constitutive elements of an IR oven such as multiple lamps (various geometries) and reflectors (ceramic or metallic). The trajectories of these rays are computed until they go away from the preform. The emitted rays which do not touch the preform is considered lost.

For ray tracing simulation, the model of the quartz tungsten halogen lamps is established. For each lamp, both the tungsten filament and the quartz tube are taken into account as two independent sources. These sources are assumed to be isotropic emission bodies. Thanks to this assumption, the discretization of the rays is performed adopting a stochastic approach. In this approach, the location for an emitted ray from either source (filament or quartz tube) is chosen randomly from two uniform number distributions: one determining the location along the lamp axis and the other determining the location on the circumference. Moreover, a stochastic approach is also applied for the definition of the ray direction vectors, allowing a numerous number of rays emitted randomly from the cylindrical surface of the sources. The further explanations about these stochastic approaches for the discretization and the direction vectors of the rays in RAYHEAT can be found in Ref. [11]. The power of the emitted energy assigned to each ray is determined by dividing the total amount of the emitted energy by the number of rays. For the quartz tube, this is calculated by Eq. (6):

$$P_{ray,q}=\frac{\varepsilon_q\left(T_q\right)S_q\sigma\left(T_q^4-T_\infty^4\right)}{N_{ray}} \tag{6}$$

where $T_\infty$ is the temperature of the air far away from the lamp, $N_{ray}$ is the number of rays emitted from the source, $S$ is the emission surface, and $\sigma$ is the Stefan–Boltzmann coefficient : $\sigma=5.67\times10^{-8}$ W m$^{-2}$ K$^{-4}$. In this application, each source has 2 million rays for tracing simulation. This number of ray is chosen regarding the previous work of Cosson et al. [11], which carried out a convergence analysis on the impact of the number of rays using RAYHEAT with respect to the calculation of view factor between a plate and a tube.

In the case of tungsten filament, a small amount of the radiation energy emitted from the source is absorbed by the quartz tube, then only the transmitted part is taken into account, Eq. (7):

$$P_{ray,f}=\frac{\tau_q\left(T_f\right)\varepsilon_f\left(T_f\right)S_f\sigma\left(T_f^4-T_\infty^4\right)}{N_{ray}} \tag{7}$$

where $\tau$ is the integrated transmissivity of the quartz.

The change in the direction of each ray at the air/ polymer interface due to refraction is computed based on the Snell-Descartes law. The calculated value of the refractive index in this study is taken equal to 1.7 [11]. Due to the small thickness of the quartz tube (i.e. $1.25e^{-3}$ m), the refraction of rays emitted from the filament while passing through the quartz is neglected. It is worth to note that the preform having a hollow body, therefore a ray may pass through two thicknesses of material before leaving the preform. In RAYHEAT, the polymer is assumed to be a cold medium, whose self-emission is neglected during the heating step. Hence, once a ray intersects the preform thickness, the absorption of radiative energy inside the material is computed following the Beer–Lambert Law, according to Eq. (8):

$$\frac{dI_\lambda(s)}{ds}=-\kappa_\lambda I_\lambda(s)=-\kappa_\lambda I_\lambda(0)\,e^{-\kappa_\lambda s} \tag{8}$$

where $I_\lambda(s)$ is the spectral intensity at the depth $s$ inside the material, along the emitted direction, $ds$ is the optical path. Then, the radiative heat source is given by Eq. (9):

$$\nabla.q_r(s)=-\int_0^\infty \kappa_\lambda I_\lambda(0)\,e^{-\kappa_\lambda s}d\lambda \tag{9}$$

In RAYHEAT, the preform is discretized into a linear hexahedral mesh that contains 14700 elements (16500 nodes), with 10 nodes in the thickness direction (Fig. 9a). The radiative heat source is computed for each volumetric mesh element. For each element, the attenuated power of each ray who passes through its volume is computed by knowing the traveling distance of the ray inside the element. Afterwards, the radiative heat source absorbed inside this volumetric element is obtained by the sum of all the rays passing through it. In terms of computational cost, the ray tracing and heat source computations took about 10 min for each lamp (including two sources) using an Intel Core *i*5 processor 1.80 GHz, with 8.0 Gb of RAM.

### 4.3. Heat transfer modeling

The radiative heat source computed from RAYHEAT for each volumetric mesh element of the preform is saved as matrix data, which is then exported to a .txt file. This .txt file can be imported for thermal simulation in COMSOL Multiphysic®, where the identical mesh of the preform is transferred as well. In order to simulate the heat transfer at the bottom of the preform, the support of the preform is also included in the simulation as an aluminum body. The screwed contact surface between the support and the preform is simplified by a flat one. The conduction between the surfaces is taken into account by assuming a perfect thermal contact. The model geometry and mesh for the thermal simulation in COMSOL Multiphysic® can be seen in Fig. 9b. For the sake of clarity, only half of the model is presented.

Heat transfer model is governed by energy conservation equation:

$$\rho C_p\frac{\partial T}{\partial t}=\nabla.(k\nabla T)-\nabla.q_r \tag{10}$$

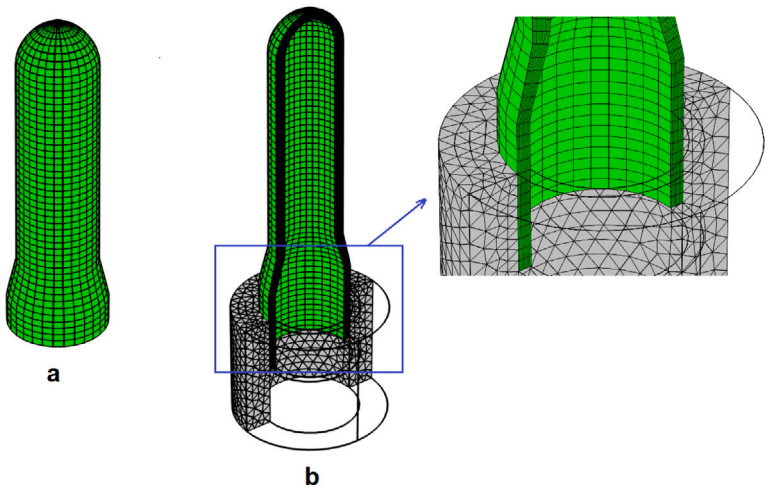


**Fig. 9.** Model geometry with its mesh. (a) 3D preform mesh in RAYHEAT, (b) half of 3D model mesh in COMSOL Multiphysic®.

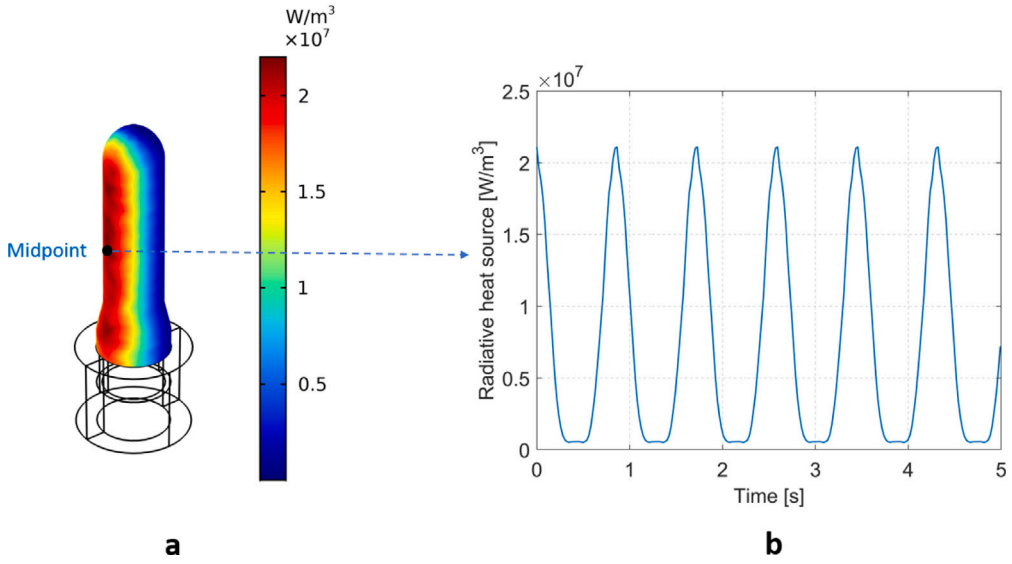


**Fig. 10.** Radiative heat source of virgin PET preform. (a) Radiative heat source distribution at $t = 0$ s; (b) Radiative heat source at midpoint vs. time.

where $\rho$ is the density, $C_p$ and $k$ are respectively the specific heat capacity (at constant pressure) and the thermal conductivity of the materials. These properties of the aluminum support are loaded from the library material contained in COMSOL Multiphysics®.

*4.3.1. Rotation of the preform*

It is worth to note that the radiative heat source computed from RAYHEAT is done for a static preform, which allows us to easily study the propagation of rays through the two thicknesses of the preform. In the experimental set-up, however, the preform rotates axially during the heating stage to ensure a uniform heating through the preform circumference. This rotation must be taken into account for thermal simulation in COMSOL Multiphysic®. Considering that the rotation of the preform in the oven is equivalent to the rotation of the oven around the preform, this rotation is done by using an interpolation function associated with a rotated coordinate system $(O, x_1, y_1, z_1)$ with respect to the reference system $(O, x, y, z)$:

$$\begin{cases} x_1 = \ \ x\cos(2\pi\omega t) + y\sin(2\pi\omega t) \\ y_1 = -\ x\sin(2\pi\omega t) + y\cos(2\pi\omega t) \\ z_1 = z \end{cases} \tag{11}$$

This interpolation function allows us to prescribe a time-dependent boundary conditions for the radiative heat source, which rotates around the preform circumference at constant speed $\omega = 1.15$ rotation per second as it can be seen in Fig. 10.

*4.3.2. Consideration of the aluminum support*

It is noted that the support is also illuminated and absorbs radiative energy from the lamps. The difference is that the aluminum support has no transmissivity, thus the opaque surface of the support can only reflect radiative energy or allow a part of it to penetrate into the substrate as an inward radiative heat flux. The determination of this radiative heat flux is much more straightforward in comparison to the one of the radiative heat source, since it does not require any information inside the material. The only supplementary parameter that is needed for this calculation is the absorptivity of the aluminum surface, which depends not only on the material but also on the surface roughness. In this work, this parameter is obtained by inverse identification. In order to do this, we perform the simulations with various value of this parameter of interest. The results are then compared with the surface temperature of the support measured by the IR thermography to figure out the best fit for the parameter. Note that it is difficult to evaluate the temperature on such a reflective metal surface by IR thermography because of its low emissivity. In fact, the temperature measurement is rather the result of a "reflection" temperature from

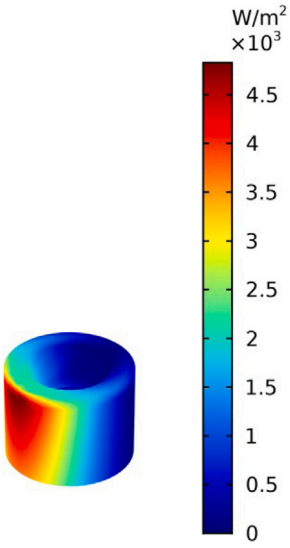


**Fig. 11.** Radiative heat flux on support surface at $t = 0$ s.

the other radiative contributions present in the oven or in its vicinity. In order to remedy this problem, we apply a small ring of black paint (5 mm high) on the aluminum support in order to identify on a high emissivity coating and therefore less sensitive to reflections, the temperature of this aluminum surface. Finally, the determined value of the absorptivity of the aluminum surface is $\alpha_a = 0.2$. Result of the heat flux of absorbed energy on the support surface is presented in Fig. 11.

#### 4.3.3. Natural convection modeling

The natural convection cooling is now considered. A previous study in the literature [17] showed that during the heating stage, the air temperature inside the preforms evolves very quickly, especially of the same order of magnitude as one of the inner surface of the preform. For this reason, the inner surfaces of both the preform and the support are considered to be adiabatic. Nevertheless, at the outer surfaces of the materials, the following heat flux boundary condition is prescribed:

$$q = h_i \left(T_i - T_\infty\right) + \varepsilon_i \sigma \left(T_i^4 - T_\infty^4\right) \quad ; \quad i = p, a \tag{12}$$

where $h$ is the convective heat transfer coefficient, $\varepsilon$ represents the integrated emissivity of materials at their own temperature. The subscripts $p$ and $a$ are used to refer the properties of polymer and aluminum respectively. $T_\infty$ is the temperature of the air far away from the perform. In Eq. (12), the first term is due to the cooling by natural convection, while the second one is due to the surface-to-ambient radiative emission. These heat losses are considered to be less important during the heating step, but it becomes critical throughout the cooling stage.

In this study, the natural convection is modeled using two different approaches. The first one solves the time-dependent energy conservation equation using a simplified heat transfer coefficient, $h$, correlated for vertical thin cylinder as proposed in Ref. [26]. The advantage of this approach is its computational parsimony, as a single coefficient is used to model the entire heat losses by convection. However, it can be insufficient if the fluid dynamics around the preform are complex (i.e. pulsed air, cycling due to closed oven), as this coefficient depends on the fluid's material properties, the surface temperature, and the geometrical configuration. The second approach refers to Computational Fluid Dynamics (CFD), which computes the convective velocity field around the preform in detail. It is then the most accurate but also the most costly in terms of computational time and memory requirement. The comparison proposed in this section helps us to choose the appropriate method.

Let define the Reynolds number $Re = \frac{\rho U L}{\mu}$, where $\rho$ is the density of air, $U$ is the air velocity, $L$ the characteristic length of the air flow (i.e. the preform diameter $L = 20$ mm) and $\mu$ the air dynamic viscosity. In natural convection, the air flow is driven by buoyancy forces induced by temperature differences together with the thermal expansion of the fluid. Considering the maximum temperatures of the preform surface, the air velocity can be considered as less then 1 m/s. Then Reynolds number is defined in the interval: $Re < 4000$, corresponding to the laminar regime.

For the first approach, the convection heat transfer coefficient, $h$, is then computed internally in COMSOL Multiphysic® according to the following equation [26]:

$$h = \frac{k}{H}\left(\frac{4}{3}\left(\frac{7Ra_H \,\mathrm{Pr}}{5\,(20 + 21\,\mathrm{Pr})}\right)^{\frac{1}{4}} + \frac{4\,(272 + 315\,\mathrm{Pr})\,H}{35\,(64 + 63\,\mathrm{Pr})\,D}\right) \tag{13}$$

where $D$ is the cylinder diameter ($D = 20$ mm), $H$ is the cylinder height ($H = 80$ mm), $Pr = \frac{\mu C_p}{k}$, $Ra_H = \frac{-g\frac{1}{\rho}\left(\frac{\partial \rho}{\partial T}\right)(T_s - T_\infty)H^3}{k\mu}$, $g$ is the acceleration of gravity, $k$ and $C_p$ are respectively the thermal conductivity and the specific heat capacity of the air, $T_s$ is the temperature of the hot material surface. It is noted that the term $-\frac{1}{\rho}\left(\frac{\partial \rho}{\partial T}\right)$ corresponds to the coefficient of thermal expansion of the air, which is evaluated at $T = \left(T_s + T_\infty\right)/2$.

The second approach solves for both the energy conservation equation and the Navier–Stokes equations for the flow of the outside cooling air within a finite control volume around the preform. The model geometry and mesh using for this simulation in COMSOL Multiphysic® can be seen in Fig. 12. The mesh convergence study was performed which showed that the temperature profiles along the preform height converged as the mesh size decreased. For the converged mesh, the air domain is meshed using 168109 elements with 5 boundary layers at the walls.

*Flow Boundary Conditions*

- An open boundary is applied for the flow on the top and lateral boundaries.
- All other boundaries (i.e. the preform and support surfaces and the bottom) are used the no slip condition.
- The preform and support surfaces are imposed a rotated velocity with respect to the rotational velocity of the preform.

*Thermal Boundary Conditions*

- On the top and lateral boundaries, an open boundary is also used, which allows free incoming flow with ambient temperature $T_\infty = 25\,°C$ and leaving flow with *a priori* unknown temperature.
- The bottom is assumed to be perfectly insulated.
- All other boundary conditions (including radiative heat source inside the preform, radiative heat flux on the support surface and heat losses due to radiative self-emission) are remained the same as in the first approach.

## 5. Results and discussion

### 5.1. Heat source analysis

The temperatures and the emitted radiative energy computed for the six quartz tungsten halogen lamps used in the experimental set-up are provided in Table 4. It is noted that the mutual heating between the lamps is not taken into account in this study. As can be seen from this table, the electrical-radiative efficiency of the IR lamps is also dependent on the electrical power input to the lamps, with a minimum radiative efficiency of 83.6% calculated at 300 W and a maximum of 89.6% at maximum electrical power 1000 W. Furthermore, the radiative energy emitted from the quartz tube is not of a negligible amount. In comparison with the radiative energy emitted from the tungsten filament, this amount accounts for 6.9% to 12.5% depending on the

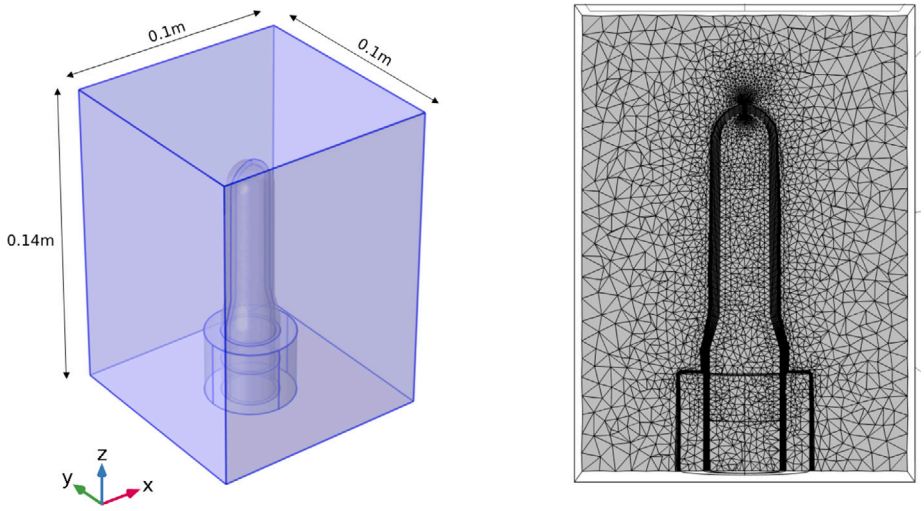


**Fig. 12.** Model geometry and mesh using for CFD approach.

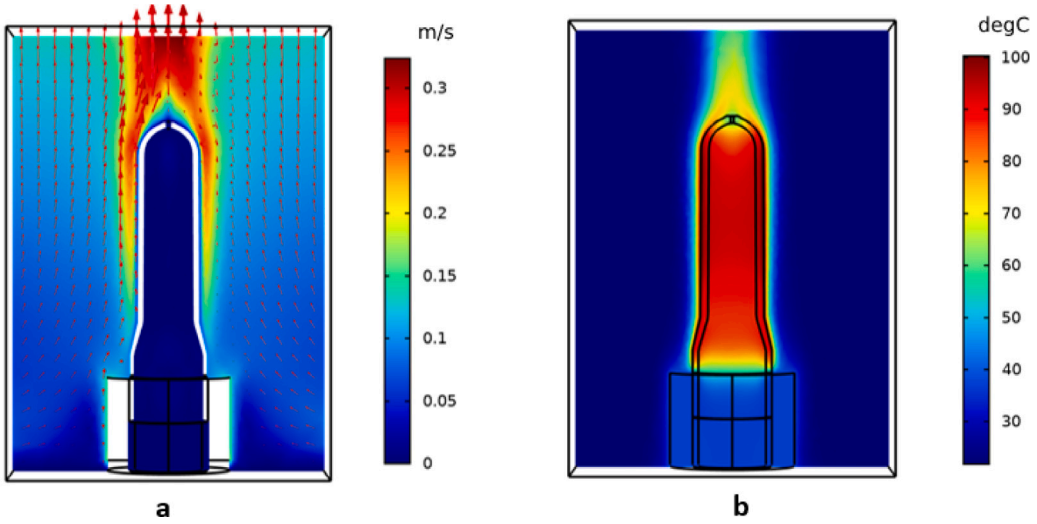


**Fig. 13.** Simulated results of CFD approach at $t = 50$ s (a) Velocity field (b) Temperature field.

**Table 4**
Summary of energy calculations for lamps.

| Parameter | Symbol | Unit | $L_1$ | $L_2$ | $L_3$ | $L_4$ | $L_5$ | $L_6$ |
|---|---|---|---|---|---|---|---|---|
| Electrical power | $P$ | $W$ | 1000 | 1000 | 450 | 300 | 750 | 900 |
| Filament temperature | $T_f$ | $K$ | 2433.4 | 2433.4 | 2035.9 | 1858.6 | 2281.9 | 2376.7 |
| Quartz temperature | $T_q$ | $K$ | 675.9 | 675.9 | 584.9 | 547.3 | 640.2 | 662.4 |
| Emitted radiative energy of filament | $P_f$ | $W$ | 838.4 | 838.4 | 352.0 | 223.0 | 615.6 | 749.1 |
| Emitted radiative energy of quartz tube | $P_q$ | $W$ | 57.6 | 57.6 | 35.3 | 27.8 | 48.2 | 54.0 |
| Electrical-radiative efficiency of filament | $P_f/P$ | % | 83.8 | 83.8 | 78.2 | 74.3 | 82.1 | 83.2 |
| Electrical-radiative efficiency of quartz tube | $P_q/P$ | % | 5.8 | 5.8 | 7.8 | 9.3 | 6.4 | 6.0 |
| Electrical-radiative efficiency of lamp | $(P_f + P_q)/P$ | % | 89.6 | 89.6 | 86.1 | 83.6 | 88.5 | 89.2 |
| Percentage $P_q/P_f$ | $P_q/P_f$ | % | 6.9 | 6.9 | 10.0 | 12.5 | 7.8 | 7.2 |

supplied electrical power to the lamp. These calculated results are consistent with the finding of Monteix et al. [17] mentioned above, who concluded that the quartz tube contributes to 9% of emitted power from the filament. Using these data, the radiative heat sources absorbed inside the PET preform and on the surface of the aluminum support are computed thanks to ray tracing analysis. Results of these computations were presented above in Figs. 10 and 11. In Fig. 10b, it was shown that the rotation of the preform induces a periodic boundary condition for heat source at a midpoint located at 40 mm from the neck, on the outer surface of the preform.

### 5.2. Natural convection analysis

Fig. 13 depicts the velocity and the temperature fields calculated from the model using CFD approach. This model describes in detail the buoyancy-driven flow of air around the preform. As can be seen from this figure, the hot preform drives vertical air currents along its walls. In order to compare the two approaches, a comparison of the predicted distribution of the convective heat transfer coefficient, $h$, along the height of the preform between the two approaches is presented in Fig. 14. Also, the temperature profiles along the preform height of

**Table 5**
Efficiency of the IR heating process.

| | Symbol | Unit | Virgin PET | 50% rPET | 100% rPET |
|---|---|---|---|---|---|
| Total radiative energyabsorbed inside the preform | $P_u$ | $W$ | 27.07 | 30.06 | 31.70 |
| Total electrical power (6 lamps) | $P_e$ | $W$ | 4400 | 4400 | 4400 |
| Volumetric average temperature of the preform at the end of heating | $\overline{T}_h$ | $°C$ | 87.31 | 92.60 | 94.88 |
| Efficiency of heating | $\eta$ | % | 0.615 | 0.683 | 0.720 |

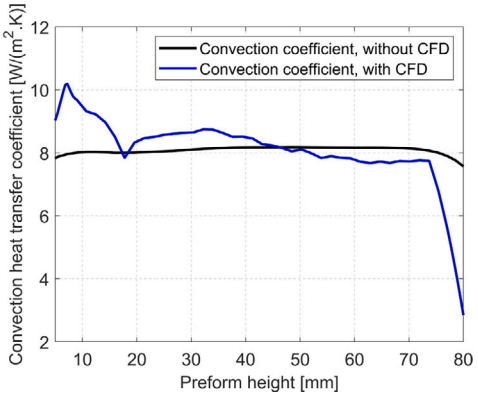


**Fig. 14.** Heat transfer coefficient along the preform height at the end of cooling stage.

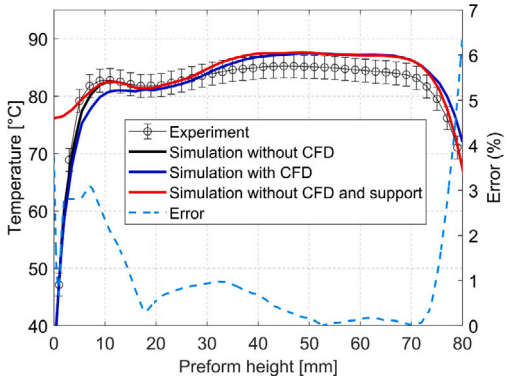


**Fig. 15.** Comparison of simulations with and without CFD at the end of cooling stage.

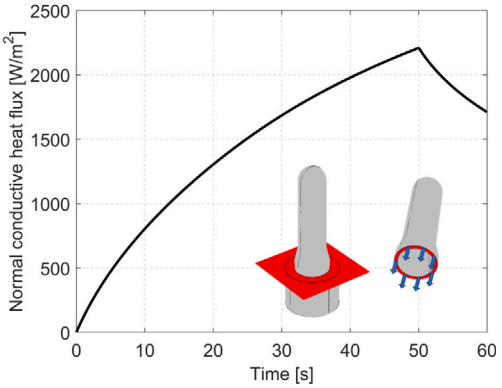


**Fig. 16.** Average normal conductive heat flux on preform bottom surface vs. time.

both approaches are plotted in Fig. 15, which can see that both results produce almost the same curve. However, the second approach predicts more in details the local effects of air flow surrounding the preform. The relative error between the two computational approach results along the preform height is almost less than 3%. This value is of the same order of magnitude as that of the measurement uncertainties (i.e. ≈ 2%). Moreover, in terms of computational cost, it took about only 15 min for the first approach, against about 10 hours for the second one using the same machine AMD Ryzen Threadripper 3960X 24-Core Processor, with 64.0 Gb of RAM. For this reason, in this study, for the specific case of natural convection, the predefined heat transfer coefficient is hereafter used to reduce the computation cost as well as to quickly achieve simulation results.

### 5.3. Thermal leakage via aluminum support

Previous studies in the literature [7,11] have often simplified boundary conditions at the bottom of the preform by prescribing an insulated surface. One of the novelties of this study is the taking into account of the heat exchange with the support aluminum in the model. This allows us to achieve more precise temperature profiles near to the preform neck. In order to consider this argument, the evolution of the average normal conductive heat flux on the preform bottom surface versus time is plotted in Fig. 16. As can be seen from the figure, this heat flux monotonic increases with time during the heating stage. This can be explained by the difference in the degree of radiative heat absorption between the semi-transparent polymer above and the aluminum surface below. Effect of this heat flux on the final temperature profile of the preform is shown above in Fig. 15, where a comparison between simulations with and without the support is plotted. It is clearly seen that, without a leakage via aluminum support, the temperature profiles near to the preform neck was overestimated.

### 5.4. Confrontation between simulation and experiment

In Fig. 17, the evolution of the temperature versus time computed at the midpoint and the temperature profiles along the preform height at the end of the heating and the cooling stages are plotted. For the sake of clarity, the plots of three material grades are separated to achieve more accurate comparisons. As can be seen from the figure, there is a good agreement between simulations and measurements. The results show that the model successfully predicts the heat-up rate during the IR heating stage. This also confirms that the radiative heat sources were well predicted by ray tracing method. Also, it is shown that the temperature distribution along the preform height are well predicted since the curving shapes are very similar. Except that there is a visible discrepancy in the area of 5–30 mm height of the preform at the end of the heating stage. This can be attributed to the fact that a certain amount of flux reflected by the preform from the support aluminum leads to an overestimation of the measurement during the heating stage. Conversely, this is depleted immediately at the cooling stage when lamps are turned off. At the end of the cooling stage, the maximum relative error is less than 5% for all the three material grades.

### 5.5. Influence of recycling rate

For the sake of comparison, simulation results of the three material grades are plotted together in Fig. 18. It is easy to see that the recycled preforms are heated more than the virgin ones. At the end of the heating stage, the temperature obtained is about 8 °C higher for 100% rPET grade than for the virgin one. These results are consistent with the absorption coefficient level of polymer grades found in Section 2.3 (Fig. 4), which showed that the recycled grades absorb more radiative

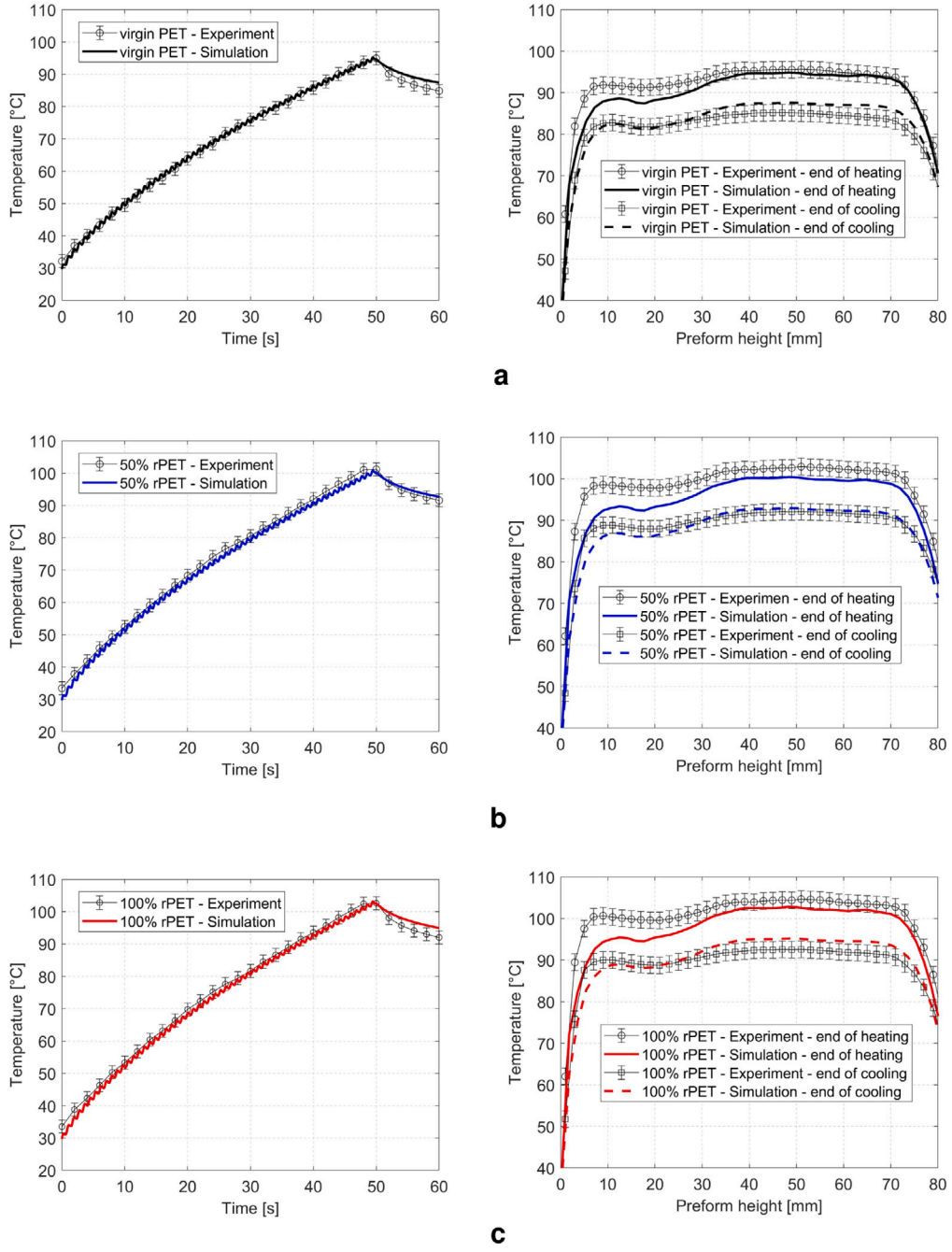


**Fig. 17.** Comparison of simulation results and measurement results (a) virgin PET (b) 50% recycled PET (c) 100% recycled PET.

energy than the virgin one, especially in the visible and near-infrared (NIR) spectra (i.e. the maximum spectral range of the IR lamp). It is noticeable that the periodic fluctuation observed in the external curve results from the rotation of the preforms. Additionally, it is noteworthy that the temperature on the inner surface becomes higher than on the outer surface after about 3 seconds of cooling. This can be explained by the fact that in the absence of the incident radiation emitted from the lamps, the heat losses due to the natural convection and the surface-to-ambient radiative emission become crucial on the outer surface, whereas the inner surface is still heated by heat conduction due to the temperature gradient within the preform wall thickness at the end of the heating stage. Moreover, the stagnation of air inside the preform prevents the internal wall to be cooled by convection, contrarily to the external preform wall. This temperature gradient is showed in Fig. 19. It can also be seen that at the end of the cooling stage, the temperature difference is approximately 4 °C. Indeed, this nonuniform temperature profile through the preform thickness is necessary to ensure a good uniformity of the stress distribution through the thickness of the bottle during the SBM process [7]. Therefore, controlling of this parameter by suitable convective conditions will be the key success factor for optimization the SBM process. Using numerical approach, it will be an interesting perspective to couple this thermal model to a mechanical one via a deformation simulation of the blowing process.

### 5.6. *Energy saving*

In order to investigate the effects of recycling on the efficiency of the IR heating stage, a summary of the energy of the different material grades is presented in Table 5. This table also shows the very low efficiency of the IR heating stage. It is important to note that these

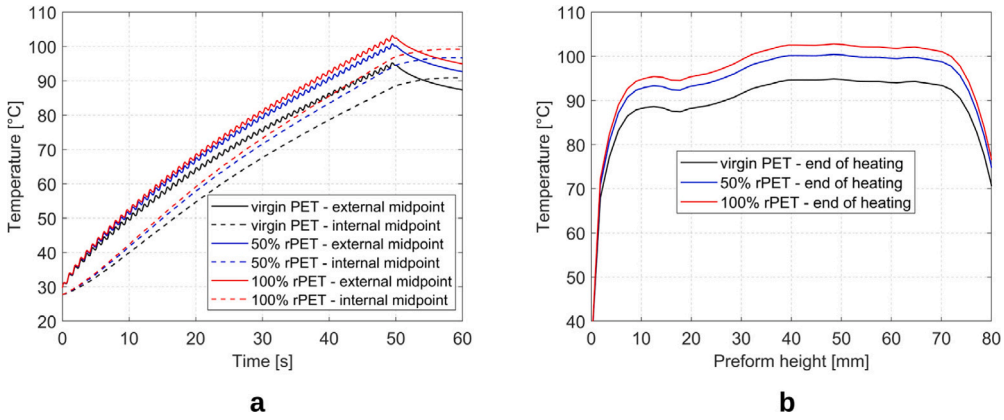


**Fig. 18.** (a) External and internal temperature vs. time at mid-height of preform (b) External temperature profile along the preform height at the end of heating.

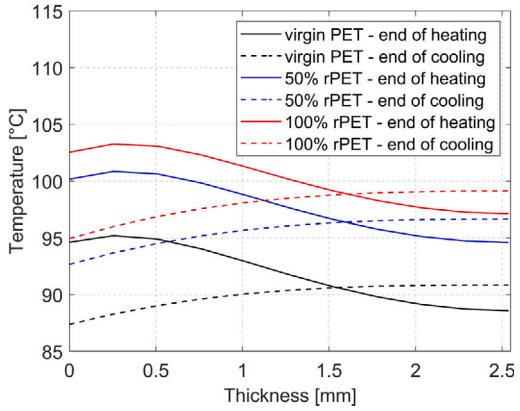


**Fig. 19.** Temperature gradient within the preform wall thickness.

efficiencies of the heating are calculated for our laboratory scale oven, where only one preform is heated each time. However, for a real industrial oven, about 10 preforms could be heated at the same time in each oven, so that these efficiencies could be *a prori* multiplied by 10 times. Based on the data from Table 5, a preliminary calculation of the energy cost of an industrial ISBM machine with respect to the three type of material grades is performed. Considering that one enables production with a capacity of up to 30000 bottles per hour, and that each preform needs to be heated to achieve an volumetric average temperature of 100 °C to be transformed. The total energy required for heating can be calculated as follows:

$$E_u = N \times \frac{P_u t_h \overline{T}_{obj}}{\overline{T}_h} \tag{14}$$

where $N$ is the number of preforms, $t_h$ is the heating time, and $\overline{T}_{obj}$ is the objective volumetric average temperature. Then, the total energy cost is calculated according to Eq. (15):

$$E = \frac{E_u}{\eta} \tag{15}$$

where $\eta$ is the efficiency of the oven. Results of these calculations for the three material grades is presented in Table 6. It can be shown that in comparison to the virgin PET, the 50% rPET and the 100% rPET gain about 5.71% and 7.98% of the total energy cost respectively. These values are not included within the measurement uncertainties (i.e. $\approx 2\%$).

## 6. Conclusion

Recycling of PET influences the optical properties of the rPET preform. Consequently, there is an impact on the efficiency of the IR heating process. In this study, we have carried out that these influences can be found essentially in the visible and near-infrared (NIR) spectra of light. In fact, the preforms become more haze with increasing levels of recycled contents.

**Table 6**
Energy cost of industrial ISBM machine.

| | Symbol | Unit | Virgin PET | 50% rPET | 100% rPET |
|---|---|---|---|---|---|
| Total energy required | $E_u$ | $kW/h$ | 12.92 | 13.53 | 13.92 |
| Efficiency of oven | $\eta$ | % | 6.15 | 6.83 | 7.20 |
| Total energy cost | $E$ | $kW/h$ | 209.98 | 197.98 | 193.22 |

In a second step, we have presented a numerical model to simulate the thermal conditioning stage of the preforms in ISBM process, taking into account the differences in optical properties between the virgin and the recycled PET preforms. In this model using ray tracing method, PET is assumed to be a non-scattering and cold medium. Thus, the absorbed radiative energy inside the preform is taking into account with the Beer–Lambert's law computed within each volumetric mesh element. The proposed model is able to predict suitably the temperature distribution of the preforms at the end of the thermal conditioning stage. In addition, the modeling of halogen lamp provides understandings of the contributions of the radiation emitted by the lamp elements over the wavelength spectrum. The natural convection is modeled using two different approaches. The CFD approach provides detailed information of the air flow around the preform. However, it is more complex and requires more computational resources than the first approach using a classical heat transfer coefficient. On the other hand, the first approach results in a rather simple model that predicts the stationary cooling well and produces accurate results for temperature distribution, which is eventually used to reduce the computation cost as well as to quickly achieve simulation results. Nevertheless, it will be an interesting perspective for the CFD approach to predict more complex air flow inside the industrial ovens, where the ventilation fan system is presented.

Finally, a summary of energy is provided by analyzing of the source term and its effect on the useful energy actually used to heat the preforms. This allows for a preliminary analyze of the efficiency of the IR heating process and subsequently for calculations the energy cost for the industrial ISBM machines.

Future work will aim to further extend the applications of the model to the industrial ovens, where the translation of the preforms across multiple ovens needs to be taken into account. In addition, the presence of the ventilation system yields a forced convective condition inside the ovens. In this context, the model with CFD approach could improve our knowledge of the convection cooling inside the ovens.

## CRediT authorship contribution statement

**Anh-Duc Le:** Conceptualization, Methodology, Software, Resources, Validation, Formal analysis, Investigation, Writing – original draft. **Rémi Gilblas:** Methodology, Investigation, Validation, Supervision, Writing – review & editing. **Vincent Lucin:** Validation. **Yannick Le Maoult:** Methodology, Investigation, Validation, Supervision, Writing – review & editing. **Fabrice Schmidt:** Methodology, Investigation, Validation, Supervision, Writing review & editing.

## Data availability

Data will be made available on request.

## Acknowledgments

The authors gratefully acknowledge the financial support from ARMINES organization for the CARNOT 2020 AAP 2 BOUTEILLE project.

## References

[1] N. Torres, J.J. Robin, B. Boutevin, Study of thermal and mechanical properties of virgin and recycled poly(ethylene terephthalate) before and after injection molding, Eur. Polym. J. 36 (10) (2000) 2075–2080, http://dx.doi.org/10.1016/S0014-3057(99)00301-8.

[2] F. Alvarado Chacon, M.T. Brouwer, E.U. Thoden van Velzen, Effect of recycled content and rPET quality on the properties of PET bottles, Part I: Optical and mechanical properties, Packag. Technol. Sci. 33 (9) (2020) 347–357, http://dx.doi.org/10.1002/PTS.2490.

[3] R. Nisticò, Polyethylene terephthalate (PET) in the packaging industry, Polym. Test. 90 (2020) 106707, http://dx.doi.org/10.1016/J.POLYMERTESTING.2020.106707.

[4] G. Venkateswaran, M.R. Cameron, S.A. Jabarin, Effects of temperature profiles through preform thickness on the properties of reheat-blown PET containers, Adv. Polym. Technol. 17 (3) (1998) 237–249, http://dx.doi.org/10.1002/(SICI)1098-2329(199823)17:3.

[5] S. Monteix, F. Schmidt, Y. Le Maoult, R. Ben Yedder, R.W. Diraddo, D. Laroche, Experimental study and numerical simulation of preform or sheet exposed to infrared radiative heating, J. Mater Process. Technol. 119 (1–3) (2001) 90–97, http://dx.doi.org/10.1016/S0924-0136(01)00882-2.

[6] Y.M. Luo, L. Chevalier, F. Utheza, X. Nicolas, Simplified modelling of the infrared heating involving the air convection effect before the injection stretch blowing moulding of PET preform, Key Eng. Mater. 611–612 (2014) 844–851, http://dx.doi.org/10.4028/WWW.SCIENTIFIC.NET/KEM.611-612.844,

[7] M. Bordival, F. Schmidt, Y.L. Maoult, V. Velay, Optimization of preform temperature distribution for the stretch-blow molding of PET bottles: Infrared heating and blowing modeling, Polym. Eng. Sci. 49 (4) (2009) 783–793, http://dx.doi.org/10.1002/PEN.21296.

[8] Y.C. Hsieh, M.H. Doan, C.M. Hung, Estimation for temperature distribution of PET preform surface under multiple lamps, Appl. Mech. Mater. 764–765 (2015) 269–273, http://dx.doi.org/10.4028/WWW.SCIENTIFIC.NET/AMM.764-765.269,

[9] B. Demirel, F. Daver, Experimental study of preform reheat temperature in two-stage injection stretch blow molding, Polym. Eng. Sci. 53 (4) (2013) 868–873, http://dx.doi.org/10.1002/PEN.23333.

[10] B. Saggin, M. Tarabini, D. Scaccabarozzi, L. Cornolti, H. Giberti, G. Moschioni, Non-contact measurement of the temperature profile of PET preforms, Measurement 133 (2019) 412–420, http://dx.doi.org/10.1016/J.MEASUREMENT.2018.10.044.

[11] B. Cosson, F. Schmidt, Y. Le Maoult, M. Bordival, Infrared heating stage simulation of semi-transparent media (PET) using ray tracing method, Int. J. Mater. Form. 2010 4:1 4 (1) (2010) 1–10, http://dx.doi.org/10.1007/S12289-010-0985-8.

[12] M. Pettersson, S. Stenström, Modelling of an electric IR heater at transient and steady state conditions: Part I: model and validation, Int. J. Heat Mass Transfer 43 (7) (2000) 1209–1222, http://dx.doi.org/10.1016/S0017-9310(99)00201-X.

[13] F. Schmidt, J.-F. Agassant, M. Bellet, Experimental study and numerical simulation of the injection stretch/blow molding process, Polym. Eng. Sci. 38 (9) (1998) 1399–1412, http://dx.doi.org/10.1002/PEN.10310.

[14] J. Howell, M. Mengüç, R. Siegel, Thermal Radiation Heat Transfer, sixth ed., CRC Press, 2015.

[15] A.C.A. Asséko, B. Cosson, F. Schmidt, Y.L. Maoult, E. Lafranche, Laser transmission welding of composites-Part A: Thermo-physical and optical characterization of materials, Infrared Phys. Technol. 72 (2015) 293–299, http://dx.doi.org/10.1016/J.INFRARED.2015.02.004.

[16] Y.L. Maoult, F. Schmidt, Infrared radiation applied to polymer processes, in: Heat Transfer in Polymer Composite Materials: Forming Processes, John Wiley & Sons, Ltd, 2016, pp. 385–423, http://dx.doi.org/10.1002/9781119116288.ch13.

[17] S. Monteix, Modélisation Du Chauffage Convectoradiatif De Préformes En Pet Pour La Réalisation De Corps Creux (Ph.D. thesis), École des Mines de Paris, 2001.

[18] S. Monteix, Y.L. Maoult, F. Schmidt, J.P. Arcens, Quantitative infrared thermography applied to blow moulding process: Measurement of a heat transfer coefficient, Quant. Infrared Thermogr. J. 1 (2) (2004) 133–150, http://dx.doi.org/10.3166/QIRT.1.133-150.

[19] F.M. Schmidt, Y. Le Maoult, S. Monteix, Modelling of infrared heating of thermoplastic sheet used in thermoforming process, J. Mater Process. Technol. 143–144 (1) (2003) 225–231, http://dx.doi.org/10.1016/S0924-0136(03)00291-7.

[20] P.O. Logerais, D. Chapron, J. Garnier, A. Bouteville, Validation of a rapid thermal processing model in steady-state, Microelectron. Eng. 85 (11) (2008) 2282–2289, http://dx.doi.org/10.1016/J.MEE.2008.07.012.

[21] M.T. Brogan, P.F. Monaghan, Thermal simulation of quartz tube infra-red heaters used in the processing of thermoplastic composites, Composites A 27 (4) (1996) 301–306, http://dx.doi.org/10.1016/1359-835X(95)00056-8.

[22] P.O. Logerais, A. Bouteville, Modelling of an infrared halogen lamp in a rapid thermal system, Int. J. Therm. Sci. 49 (8) (2010) 1437–1445, http://dx.doi.org/10.1016/J.IJTHERMALSCI.2010.03.003.

[23] R. Jenkins, B. Aldwell, S. Yin, M. Meyer, A.J. Robinson, R. Lupoi, Energy efficiency of a quartz tungsten halogen lamp: Experimental and numerical approach, Therm. Sci. Eng. Prog. 13 (2019) 100385, http://dx.doi.org/10.1016/J.TSEP.2019.100385.

[24] P.C. Chang, S.J. Hwang, Simulation of infrared rapid surface heating for injection molding, Int. J. Heat Mass Transfer 49 (21–22) (2006) 3846–3854, http://dx.doi.org/10.1016/J.IJHEATMASSTRANSFER.2006.04.014.

[25] T.L. Turner, R.L. Ash, Numerical and Experimental Analyses of the Radiant Heat Flux Produced by Quartz Heating Systems, NASA Technical Paper 3387, 1994.

[26] B. Adrian, Convection Heat Transfer, fourth ed., John Wiley & Sons, 2013.